

Volcanic Satellites Tidally Venting Na, K, SO₂ in Optical & Infrared Light

Apurva V. Oza^{1,2*}, Andrea Gebek³, Moritz Meyer zu Westram⁴, Armen Tokadjian², Anthony L. Piro⁵, Renyu Hu^{2,1}, Athira Unni^{6,7}, Raghav Chari⁸, Aaron Bello-Arufe², Carl A. Schmidt⁹, Amy J. Louca¹⁰, Yamila Miguel^{10,11}, Raissa Estrela², Jeehyun Yang², Mario Damiano², Yasuhiro Hasegawa², Luis Welbanks¹², Diana Powell¹³, Rishabh Garg¹⁴, Pulkit Gupta¹⁵, Yuk L. Yung¹, and Rosaly M.C. Lopes²

¹Division of Geological and Planetary Sciences, California Institute of Technology, Pasadena, USA

²Jet Propulsion Laboratory, California Institute of Technology, Pasadena, USA

³Sterrenkundig Observatorium, Universiteit Gent, Ghent, Belgium

⁴Physikalisches Institut, Universität Bern, Bern, Switzerland

⁵The Observatories of the Carnegie Institution for Science, Pasadena, 91101

⁶Department of Astronomy & Astrophysics, University of California, Santa Cruz, USA

⁷Department of Physics and Astronomy, University of California, Irvine, USA

⁸Department of Physics and Astronomy, University of Tennessee, Knoxville, USA

⁹Center for Space Physics, Boston University, Boston, USA

¹⁰Leiden Observatory, Leiden University, Leiden, The Netherlands

¹¹SRON Netherlands Institute for Space Research, Leiden, The Netherlands

¹²School of Earth and Space Exploration, Arizona State University, Tempe, USA

¹³Department of Astronomy & Astrophysics, University of Chicago, Chicago, USA

¹⁴Portola High School, Irvine, USA

¹⁵Indian Institute of Technology, Indore, India

Accepted 4 August 2025, in press

ABSTRACT

Recent infrared spectroscopy from the *James Webb Space Telescope* (JWST) has spurred analyses of common volcanic gases such as carbon dioxide (CO₂), sulfur dioxide (SO₂), alongside alkali metals sodium (Na I) and potassium (K I) surrounding the hot Saturn WASP-39 b. We report more than an order-of-magnitude of variability in the density of neutral Na, K, and SO₂ between ground-based measurements and JWST, at distinct epochs, hinting at exogenic physical processes similar to those sourcing Io’s extended atmosphere and torus. Tidally-heated volcanic satellite simulations sputtering gas into a cloud or toroid orbiting the planet, are able to reproduce the probed line-of-sight column density variations. The estimated SO₂ flux is consistent with tidal gravitation predictions, with a Na/SO₂ ratio far smaller than Io’s. Although stable satellite orbits at this system are known to be < 15.3 hours, several high-resolution alkali Doppler shift observations are required to constrain a putative orbit. Due to the Roche limit interior to the planetary photosphere at ~8 hours, atmosphere-exosphere interactions are expected to be especially important at this system.

Key words: planets and satellites: physical evolution – planets and satellites: rings – planets and satellites: detection – planets and satellites: atmospheres – planets and satellites: dynamical evolution and stability

1 INTRODUCTION

At the time of this writing, Saturn has 274 confirmed moons in orbit, 67 of which were discovered in the past decade alone (Sheppard et al. 2018, 2023), and 128 more were reported by the Minor Planet Center on March 11, 2025 following an irregular satellite campaign at the CFHT (Ashton et al. 2025). It is now well known that Saturn’s rings are actively shaped by its natural satellites (Charnoz et al. 2018). Another splendid example is Enceladus, which actively shapes Saturn’s E-ring due to its tidally-heated hydrothermal venting, leading to a hydroxide torus of gas (Johnson et al. 2006a) and grains. Of

course, Io is well known to host a μ bar volcanic and sublimated sulfur dioxide SO₂ atmosphere observed to vary from 10^{16} - 10^{17} SO₂/cm² (Lellouch et al. 2015). In fact, SO₂ is one of the most common gases, along with CO₂ and H₂O, released in a volcanic eruption on Earth. Ongoing volcanism on Venus was only recently confirmed (Herrick & Hensley 2023; Sulcanese et al. 2024) despite its obvious atmospheric SO₂ signature with *Venus express* measurements at 0.02 ppm below 90 km and roughly 5 ppm above 100 km (Mahieux et al. 2023). In terms of discovered elements at exoplanets, the relative abundances of volatile metals, notably neutral sodium (Na I), potassium (K I) and SO₂ are well known to be sensitive to silicate lava temperatures (Fegley & Zolotov 2000), reminding us of one of their origins as silicate magmas.

* E-mail: oza@caltech.edu

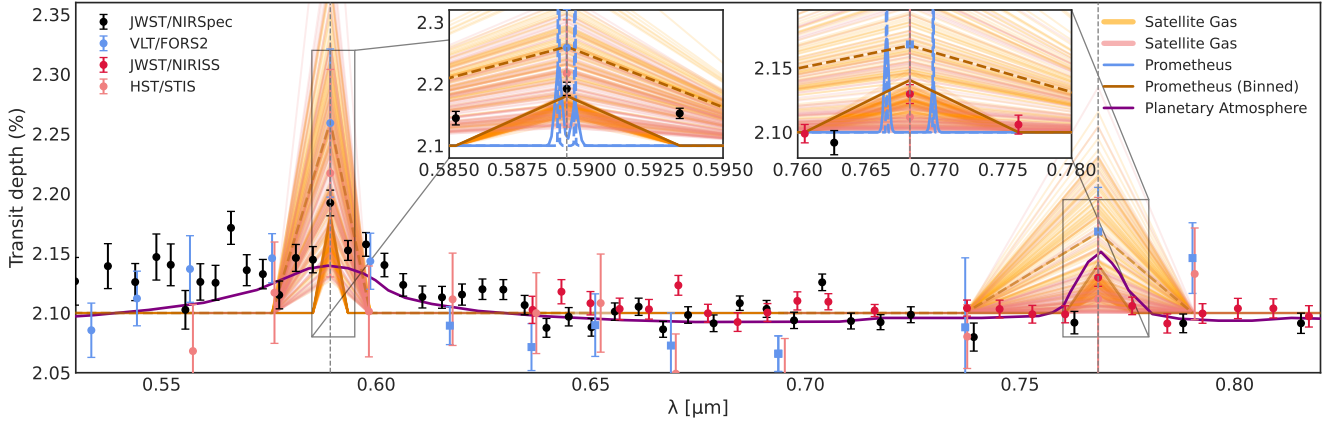


Figure 1. Alkali metals: Na I & K I as observed by the VLT (blue) (Nikolov et al. 2016), HST (pink) (Fischer et al. 2016), JWST/NIRISS (red) (Feinstein et al. 2023), and JWST/NIRSpec (black) (Rustamkulov et al. 2023), with accompanying planetary (1-D radiative-convective-thermochemical equilibrium: purple) and satellite gas (orange for VLT and JWST, pink for HST) simulated with 100 optically-thin models c.f. Eqn 1 approximating equivalent widths $W_\lambda \propto N$ (Eqn. 4) reported in Table 2. Zoom inset: promethus forward models are shown in high-resolution (satellite cloud: blue-dashed; torus: blue solid) and binned to the data (brown in the respective line styles).

Telescope (Alkali)	VLT (Na)	HST (Na)	JWST (Na)	VLT (K)	HST (K)	JWST (K)	JWST (K)
Instrument	FORS2	STIS	NIRSpec	FORS2	STIS	NIRISS	NIRSpec
Epoch	2016-3-8	2013-3-17	2022-7-10	2016-3-12	2013-3-17	2022-7-27	2022-7-10
dF_λ/F_\star (%)	$2.234^{+0.067}_{-0.067}$	$2.189^{+0.078}_{-0.050}$	$2.190^{+0.011}_{-0.011}$	$2.143^{+0.042}_{-0.039}$	$2.095^{+0.040}_{-0.021}$	$2.127^{+0.008}_{-0.008}$	$2.125^{+0.001}_{-0.001}$
$\log N$ [cm ⁻²] MCMC	$11.76^{+0.18}_{-0.28}$	$11.54^{+0.27}_{-0.33}$	$10.96^{+0.43}_{-0.10}$	$11.46^{+0.26}_{-0.61}$	$10.94^{+0.62}_{-0.63}$	$10.62^{+0.19}_{-0.17}$	$9.96^{+1.36}_{-1.36}$
σ_v [km/s]	$31.6^{+116.3}_{-25.2}$	$32.4^{+119.0}_{-25.8}$	$89.1^{+124.7}_{-50.2}$	$28.8^{+112.4}_{-22.5}$	$30.2^{+117.7}_{-23.9}$	$11.5^{+39.8}_{-9.1}$	$0.98^{+1.16}_{-0.52}$
v_{kin} [km/s]	50.5	51.6	142.2	46.0	48.2	18.3	1.56
$\log N$ [cm ⁻²] promethus	11.45 (∅)	-	10.77 (torus)	11 (∅)	-	10.38 (torus)	-
σ_v [km/s]	7.8	-	62.7	7.8	-	62.7	-
v_{kin} [km/s]	12.5	-	100	12.5	-	100	-

Table 1. Optically-thin alkali column density minima N , corresponding 1-D velocity dispersions σ_v , and approximate kinetic velocities (Eqn. 5) for MCMC posterior simulations (top; (orange in Figure 1)) and promethus models (bottom; blue, brown). Transit depths are normalized at $c = 0.0210$. Satellite cloud and tori geometries are indicated as (∅) and (torus) respectively.

In principle, if a third body were to be present at a planetary system, the natural satellite would experience tidal heating should it be in a perturbed or eccentric orbit (Peale et al. 1979).

Especially exciting is the case for a habitable-zone exomoon (Tokadjian & Piro 2023), possibly outshining the planet itself from 6-8 μm in the infrared, due to the satellite blackbody flux being boosted by tidal heating.

Novel techniques to detect infrared-bright exomoons in spectroscopy (e.g., Kleisioti et al. 2023, 2024), has spawned multiwavelength searches in radio (Narang et al. 2023a,b) and thanks to the bright sodium and potassium lines in absorption spectroscopy, visible light (Oza et al. 2019). At transiting exoplanet systems, putative exomoons are subject not only to the host planet’s gravitational tide, but also the massive gravitational field of the host star. Beyond a planetary orbit of a couple days, tides dissipate energy into the interior of the satellite due to orbital resonance, rather than decay its orbit ((Cassidy et al. 2009), see also Figure 5). The tidal field of the star and planet in concert, acting on a natural satellite, drive three-body gravitational heating, an expression derived in Cassidy et al. (2009); Oza et al. (2019) which is far larger at a close-in system than canonical eccentricity-driven tides (Peale et al. 1979). 3-body heating is

so large that gas and grain volcanism on these putative satellites is inevitable and predicted to be roughly $\sim 10^{5\pm1} \times$ the energy measured at Io (Veeder et al. 1994). As a first approximation, if the satellite has an unknown size $R_\emptyset \sim R_{Io}$, orbiting a Jupiter or Saturn-sized object over a range of orbital periods $2 \leq \tau_p \leq 5$ days (equilibrium temperatures of $\sim 1000 \leq T_{eq} \leq 2500$ Kelvins), the tidal venting rate computed by Oza et al. (2019) is roughly $\sim 10^{8\pm1}$ kg/s (more than $100 \times$ Io’s). Of course, depending on the size and magmatic state of putative rocky exomoons, thermal evaporation may also source $\dot{M} \gg 10^8$ kg/s (Oza et al. 2019). Whether this range of volcanism is observable, and whether any of these putative exomoons have survived disintegration, leads us to the current investigation of infrared data with *James Webb Space Telescope* (JWST) MIR and NIR data.

We focus on one of the farthest host planets from the sample of extrasolar-Ios studied by Oza et al. (2019) at $\tau_p \sim 4.1$ days. The distance allows for a larger Hill sphere where natural satellites are dynamically stable (Kisare & Fabrycky 2024). WASP-39 b is a highly-inflated hot Saturn orbiting a $m_K=12.11$, G7 host star located 215.4 ± 0.7 pc away (Faedi et al. 2011). Fortunately WASP-39 b has been heavily monitored in visible light (by the Hubble Space Telescope (HST/STIS) (Sing et al. 2016; Fischer et al. 2016)

Epoch	Atom	Instrument	N [cm ⁻²]	W_λ (mÅ)	$\dot{M}_{\text{tor}} - \dot{M}_\gamma$ [kg/s]
2016-03-08	Na	VLT/FORS2	$10^{11.65^{+0.19}_{-0.36}}$	131 ± 73	$(0.8 - 81) \times 10^5$
2013-03-17	Na	HST/STIS/G750L	$10^{11.60^{+0.27}_{-0.81}}$	119 ± 109	$(0.3 - 87) \times 10^5$
2022-07-10	Na	JWST/NIRSpec	$10^{10.78^{+0.11}_{-0.15}}$	17.8 ± 5.2	$(0.2 - 9.1) \times 10^4$
2016-03-12	K	VLT/FORS2	$10^{11.42^{+0.29}_{-1.43}}$	136 ± 131	$(0.7 - 380) \times 10^5$
2013-03-17	K	HST/STIS/G750L	$< 10^{10.43}$	14.0 ± 233.6	$< 35 \times 10^5$
2022-07-10	K	JWST/NIRSpec	$< 10^{10.47}$	15.5 ± 28.7	$< 6.2 \times 10^5$
2022-07-27	K	JWST/NIRISS	$10^{10.61^{+0.12}_{-0.17}}$	21.3 ± 7.0	$(0.2 - 39) \times 10^5$
Epoch	Molecule	Instrument	N [cm ⁻²]	T_{kin} (K)	$\dot{M}_{\text{tor}} - \dot{M}_\gamma$ [kg/s]
2022-07-30	SO ₂	JWST/G395H	$10^{16.7^{+0.1}_{-0.1}}$	1100^{+120}_{-110}	$(0.6 - 40) \times 10^{11}$
2022-07-10	SO ₂	JWST/NIRSpec	$10^{16.4^{+0.2}_{-0.5}}$	780^{+460}_{-330}	$(0.3 - 20) \times 10^{11}$
2023-02-14	SO ₂	JWST/MIRI	$10^{15.1^{+0.2}_{-0.5}}$	1180^{+1400}_{-690}	$(0.15 - 10) \times 10^{10}$
2022-07-30	CO ₂	JWST/G395H	$10^{15.46^{+0.03}_{-0.03}}$	2200^{+140}_{-100}	$(2.4 - 3.0) \times 10^8$
2022-07-10	CO ₂	JWST/NIRSpec	$10^{15.44^{+0.02}_{-0.02}}$	2000^{+70}_{-90}	$(2.3 - 2.9) \times 10^8$

Table 2. Optically thin column densities for various volcanic species. For atoms we report the equivalent width (W_λ) in mÅ, and for molecules we report the temperature T_{kin} in Kelvins. NIR retrievals are from 3.9–4.5 μm , MIR retrievals from 6–8 μm . Normalizations: JWST/PRISM $2.107^{+0.006}_{-0.007}$, JWST/G395H $2.089^{+0.006}_{-0.006}$, JWST/MIRI $2.108^{+0.007}_{-0.007}$. Column densities N , are estimated by transit depths as described for atoms via W_λ in §2.1 and inverse models for molecules, in §2.2. \dot{M} represents the inferred mass loss rates. γ - and torus-limited describe photoionization-limited clouds¹ and tori with $\sim 3\text{h}$ charge-exchange lifetimes.

VLT/FORS2 (Nikolov et al. 2016)), and by JWST in the near-infrared (NIR) (Wakeford et al. 2018; Rustamkulov et al. 2023; Feinstein et al. 2023; Ahrer et al. 2023; Alderson et al. 2023), and mid-infrared (MIR) (Powell et al. 2024) for 11 total epochs. In this short letter, we provide a volcanic alternative to the robust H₂S driven atmospheric photochemistry Yung & Demore (1999); Tsai et al. (2023); Yang & Hu (2024) as a source for SO₂. In this light, we determine the optically-thin Na I, CO₂, and SO₂ column densities from available data using the technique of evaporative transmission spectroscopy (Gebek & Oza 2020) in §2. Lastly, as a test case in §3 we simulate the toroidal exosphere of WASP-39 b sourced by an outgassing rate \dot{M} via the exomoon torus softwares: dishoom & serpens (Meyer zu Westram et al. 2024). Finally, we discuss implications and future outlook in §4.

2 EVAPORATIVE TRANSMISSION SPECTRA ANALYSIS

We first consider simplistic optically thin absorption from atoms and molecules in a tenuous exosphere. In this optically-thin scenario, the transit depth is directly proportional to the number of absorbing particles spread over the stellar disk, expressed as the change in stellar flux over a wavelength region λ (Draine 2011; Gebek & Oza 2020):

$$\frac{dF_\lambda}{F_\star} \approx N\sigma(\lambda), \quad (1)$$

where $\sigma(\lambda)$ is the absorption cross-section, and N (cm⁻²) the average line-of-sight (LOS) column density of the absorber. Figure 1 shows how the transit depth $\frac{dF_\lambda}{F_\star}$ near the alkali absorption lines varies between epochs (black, blue, and red data points).

As described more in Section 3 the total number of absorbing particles can be estimated by a mass loss relation:

$$N = (\dot{M}/m) \cdot \tau_\gamma \quad (2)$$

where m is the volatile mass, τ_γ is the lifetime against photoionization, approximating a *cloud* of particles limited by the ambient solar field. More generally, τ_γ can be described for an arbitrary

species τ_i and physical processes¹ (Oza et al. 2019). To approximate a *toroid* we adopt the value $\tau_{\text{tor}} \sim 3$ hours by Meyer zu Westram (2023) characteristic of charge-exchange (Johnson & Strobel 1982) and other well-known processes at Jupiter-Io plasma torus (Schmidt et al. 2023). In this way \dot{M}_γ and \dot{M}_{tor} are inferred mass loss rates to power the observed line-of-sight column densities $\bar{N} \sim \frac{N}{\pi R_\star^2}$ so that the column density is directly proportional to the mass loss rate:

$$N \sim \dot{M} \frac{\tau_i}{m_i \pi R_\star^2} \quad (3)$$

where N (Eqn. 2) can be distributed into a photoionized cloud or plasma torus geometry (Gebek & Oza 2020).

Table 2 shows (a) for atomic features, the computed column densities (Eqn. 1) for each epoch of data and equivalent widths (see Section 2.1); (b) for molecular features, column densities and temperatures (Section 2.2), and (c) mass loss rates for both atoms and molecules (as described by Eqns. 2 and 3).

2.1 Alkali Gas in the Optical

One can approximate N of neutral sodium and potassium analytically by the sum of two Voigt profiles (approximating the D₂ and D₁ alkali resonance lines). As the low-resolution data here does not resolve these absorption lines, we measured the equivalent width (W_λ) of the line relative to the continuum determined by the normalization fit to the data near the Na & K resonance lines. W_λ therefore is directly proportional to N , given by Draine (2011)

$$W_\lambda = \frac{\pi e^2}{m_e c^2} (f_{D2} \lambda_{D2}^2 + f_{D1} \lambda_{D1}^2) \times N, \quad (4)$$

where e the elementary charge, m_e the electron mass, c the speed of light, and f_D (λ_D) the oscillator strength (wavelength) of the D-line alkali transition, as also summarized in Oza et al. (2019) Eqn.

¹ $\tau_{\gamma, \text{CO}_2} = 2.3\text{h}$; $\tau_{\gamma, \text{SO}_2} = 2.5\text{m}$; $\tau_{\gamma, \text{Na}} = 6.6\text{m}$; $\tau_{\gamma, \text{K}} = 1.8\text{m}$

14. This is an approximation as discussed by [Draine \(2011\)](#) is exact for $\tau_0 \rightarrow 0$, and within 2.6 % for the optically thin $\tau_0 < 1.256$, in the limit where the term $\left(\frac{1}{1+\frac{\tau_0}{2\sqrt{(2)}}}\right)$ approaches unity. It follows that the measured equivalent width of the sodium and potassium lines are directly related to the average line-of-sight column density N reducing to the number of absorbing atoms $N \sim N\pi R_\star^2$ ([Johnson & Huggins 2006](#)) modeled in 3-D in Section 3. For each individual transit of WASP-39 b, neutral sodium & potassium column densities are simulated with 100 optically-thin models following Equation 1 indicated in orange and pink corresponding to the datasets identified in the caption, approximating the range of column densities derived from their equivalent widths following Equation 4 ([Draine 2011](#)), reported in Table 2. Prometheus simulations ([Gebek & Oza 2020](#)) (indicated in blue, brown (binned)) approximate gas density minima values provided in Table 1.

In Figure 1 we employ the radiative transfer tool **prometheus** to model the transit depth of a satellite gas source following [Gebek & Oza \(2020\)](#), distributing a packet of evaporating N particles into two distinct geometries: 1) toroid (solid blue) and 2) sputtered cloud (dashed blue). Due to the tenuous nature and limited extent of the cloud scenario, the dashed absorption lines are narrow probing mostly the line core. The planetary atmosphere (purple) is adopted from [Rustamkulov et al. \(2023\)](#) assuming chemical equilibrium in a hydrostatic atmosphere. The simulated minimum alkali column densities are computed here from Eqn. 4 (Table 2) based on the sodium and potassium data seen by VLT, HST, and JWST. Strikingly the data are not consistent within error. Moreover, we find that the equivalent width changes by a factor of 7.4 from epoch to epoch for sodium, and more than 1.3 to a surprising disappearance for potassium. Two **prometheus** models are shown in Figure 1: 1) an alkali toroid (solid blue) with a semi-major axis, $a_{\text{torus}} \sim 1.5 R_p$ and 1-D velocity dispersion $\sigma_v \sim 62.7 \text{ km s}^{-1}$, which if due to thermal motions, described in [Gebek & Oza \(2020\)](#) Eqn. 2 as a line temperature, follows a Maxwell Boltzmann distribution with average velocity: $\bar{v}_{MB} = \sqrt{\frac{8k_B T}{\pi m}}$ ([Reif 1965](#)) so that:

$$v_{kin} = \sqrt{\frac{8}{\pi}} \sigma_v \quad (5)$$

roughly 100 km/s, characteristic of energetic neutral atoms (ENAs) and plasma interactions at Jupiter-Io ([Meyer zu Westram 2023; Wilson et al. 2002](#)). Secondly, 2) an alkali cloud (dashed blue) orbiting at $0.41 R_{\text{Hill}}$ ([Kisare & Fabrycky 2024](#)) fueled by an exomoon at $a \sim 1.5 R_p$ on a $\tau \sim 15.3$ hour orbit c.f. Table 1.

Specifically, a satellite cloud (dashed orange **prometheus** line in Figure 1) with a column density of $\sim 10^{11.45} \text{ Na/cm}^2$ roughly approximates the observed VLT (blue) and HST (pink) absorption values: ($\sim 10^{11.65}$ and $\sim 10^{11.60} \text{ cm}^{-2}$, respectively), whereas the JWST/NIRSpec (black) epoch is slightly more tenuous $\sim 10^{10.78} \text{ cm}^{-2}$, roughly consistent with a torus (solid, orange **prometheus** line in Figure 1) fueled by $\sim 7.2 \times 10^{32} \text{ Na I}$ particles. In the JWST/NIRISS dataset (red), the potassium column is $\sim 10^{10.61} \text{ cm}^{-2}$, which **prometheus** simulations approximate with $\sim 3 \times 10^{32} \text{ K I}$ particles in a toroidal geometry. Although high-resolution observations are needed to quantify Na & K variability distinct from a super-stellar planetary atmosphere ([Powell et al. 2024](#)), the variability in K I is particularly stark, with detections in the VLT and JWST/NIRISS epochs ($\sim 10^{11.4} - 10^{10.6} \text{ cm}^{-2}$) contrasted by a disappearance in the JWST/NIRSpec and HST epochs (Table 2), which may be suggestive of an orbiting satellite cloud $\sim 10^{12.1}$

cm^{-2} , varying its phase along the observer's line-of-sight ([Meyer zu Westram 2023](#)).

2.2 Volcanic Gas in the Infrared

For molecular absorption in the NIR and MIR, the approximation in Eqn. 4 is more complex, as σ_λ is no longer an analytical function of wavelength, but rather a composite of many line transitions. We therefore model the observed SO_2 and CO_2 NIR and MIR transit depth $\frac{dF_\lambda}{F_\star}$ in the optically-thin limit (Eqn. 1) by computing $\sigma(\lambda)$ on a T-P-grid from the ExoMOL database ([Tennyson et al. 2024](#)) in order to infer N and its error. Assigning a temperature and a pressure to the gas is a significant simplification of the problem as the upper atmosphere or exosphere is generally not in local thermodynamical equilibrium (LTE), well known for Io's mid-infrared SO_2 bands ([Lellouch et al. 2015](#)). Here, we assume the lowest tabulated pressure value of 0.1 nbar when extracting ExoMOL opacities. We find that increasing pressure up to 0.1 μbar hardly affects the molecular opacities considered here, and are therefore representative of minima. We leave temperature as a free parameter from $T = 100\text{--}3400 \text{ K}$ and allow each absorbing species to have a different T . Additionally, we assume a constant normalization, treated as a free parameter. Overall, this leaves us with two free parameters for each absorber contributing to the observed transit depth, plus one free parameter regulating the normalization. We use flat priors for T , $\log_{10}(N/\text{cm}^{-2})$, and $\log_{10}(\sigma_v/(\text{km s}^{-1}))$. We run a **python** MCMC **emcee** sampler ([Foreman-Mackey et al. 2013](#)) with 32 walkers for 5000 steps, and discard the first 1000 steps as burn-in. The results (column densities and temperatures) from the optically-thin retrieval for the various infrared datasets are summarized in Table 2 for molecules, with the accompanying spectra and posterior distributions in Figure 2. Whereas an extended atmosphere of WASP-39 b is expected to return a consistent signal across planetary transit epochs, an exomoon orbit naturally leads to order-of-magnitude changes in column density and, consequently, spectral transit depth. For instance the SO_2 flux from the 2022-07-30 epoch to 2023-02-14 has varied from $N_{\text{SO}_2} \sim 10^{16.7 \pm 0.1}$ to $N_{\text{SO}_2} \sim 10^{15.1^{+0.2}_{-0.5}} \text{ SO}_2/\text{cm}^2$, far larger than the CO_2 variability. Indeed, the CO_2 appears to be consistent despite the optically-thin approximation on average near $\sim 10^{15.45 \pm 0.03} \text{ CO}_2/\text{cm}^2$ implying the SO_2 is indeed suggestive. Although, WASP-39 has not been reported to be active ([Faedi et al. 2011](#)), 2/14 exomoon candidates from the [Oza et al. \(2019\)](#) sample, highlight sources of variability worth considering. Star spot crossings at WASP-52 were shown to modulate H_2O abundances ([Fournier-Tondreau et al. 2025](#)), while at WASP-31 b puzzling detections and non-detections of K I by the VLT in both low and high-resolution spectroscopy were reported to be instrumental, albeit with no systematic identified ([Gibson et al. 2019](#)). Multi-epoch observations with the same instrument are therefore essential to characterize variability. Indeed at the volcanic exoplanet candidate, 55 Cancri-e ([Quick et al. 2020](#)), toroidal behavior near 4 microns is seen across multiple epochs with the same JWST instrument ([Patel et al. 2024](#)). We now use the optically thin analytic and **prometheus** forward models as a benchmark for detailed Na, K, and SO_2 3-D Monte Carlo simulations of the approximate toroidal gas geometry in the next section.

3 NUMERICAL ESTIMATES OF VOLCANIC GAS DENSITIES

In addition to fitting the NIR and MIR observations as described in Section 2, we employ the test-particle Monte-Carlo code **serpens** ([Meyer zu Westram 2023; Meyer zu Westram et al. 2024](#)) for first-order simulation analysis in Figure 3. We infer Na, K, and SO_2

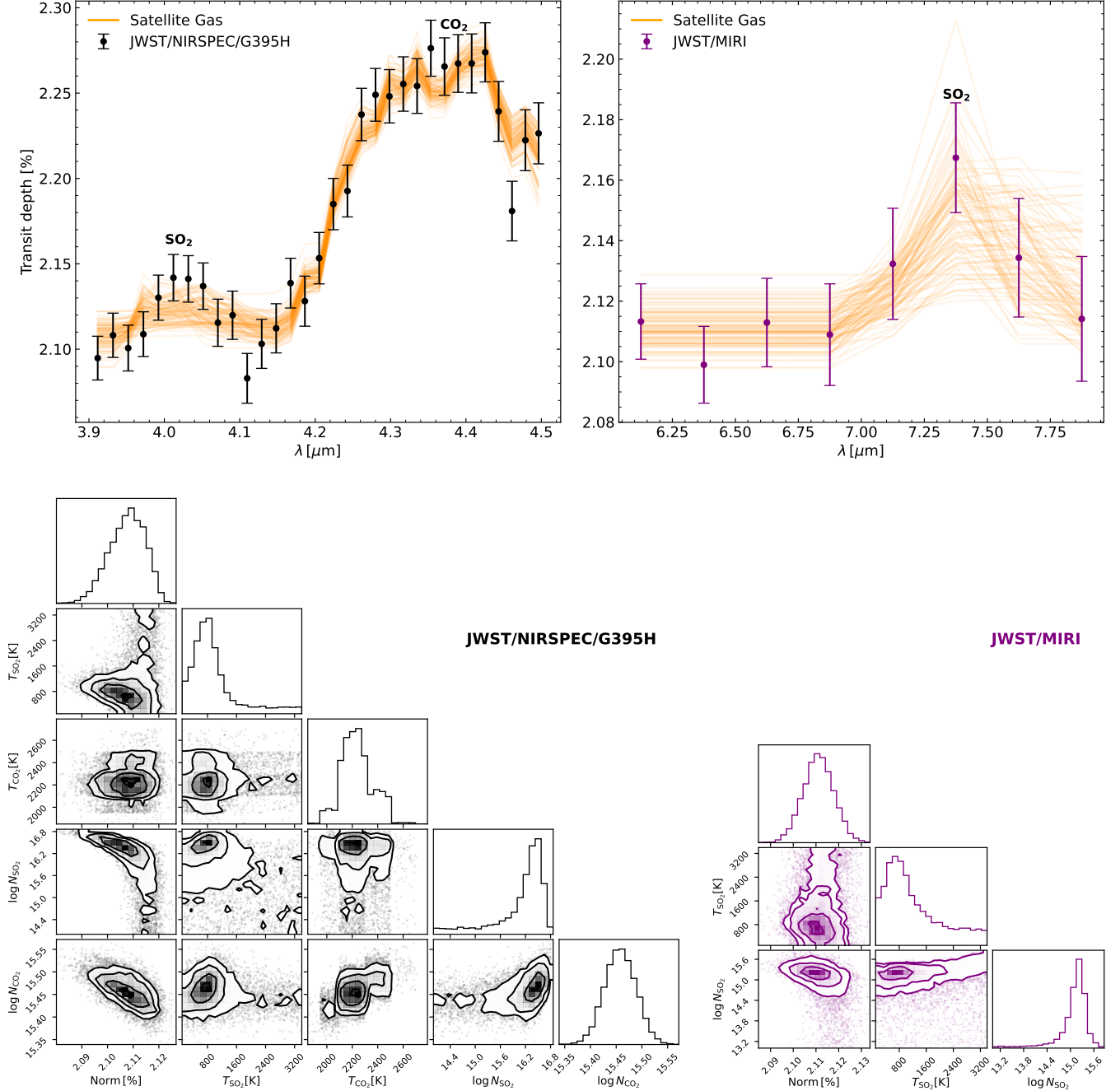


Figure 2. *Top panel:* 100 optically-thin transmission spectra models of SO_2 and CO_2 gas in orange, with central values listed in Table 2. *Bottom panel:* Posterior distributions, including the temperature T of the gas, column density N , and normalization. JWST NIR data is in black and MIRI in purple.

particle- and line-of-sight densities at regular time intervals from the WASP-39 b system which is simulated with the inclusion of a putative exomoon WASP-39 b I as the particle source. We distinguish between a cloud and toroidal scenario as described in §2 on evaporative transmission spectroscopy analysis, where the

density computations are normalized by maintaining a constant total number of atoms N of mass m in the simulation following the analytical approximation in Eqn. 2.

Considering the proximity of the star, we incorporate radiation pressure forces following the methodology outlined in Meyer zu Westram et al. (2024). We primarily consider $R_{\text{J}} \sim R_{\text{Io}}$, although a

terrestrial-sized volcanic satellite (e.g. Bello-Arufe et al. (2025)) is also considered in Figure 4iii. Through analyzing the systems' evolution over time, we derive density *phase-curves* that illustrate the average particle and line-of-sight densities at any point in time over the duration of one exomoon's orbit. Results for Na limited by photoionization at higher velocities yield an elongated cloud reminiscent of the Io Banana cloud (Smyth & Combi 1988; Wilson et al. 2002) (see Figure 3). Albeit, the exomoon cloud is more localized and lacks a complete toroidal structure due to short particle lifetimes. The on-line version of this manuscript provides a time-series sequence of Na evolution for both tori (Fig. 3a) and cloud (Fig. 3b) scenarios. The

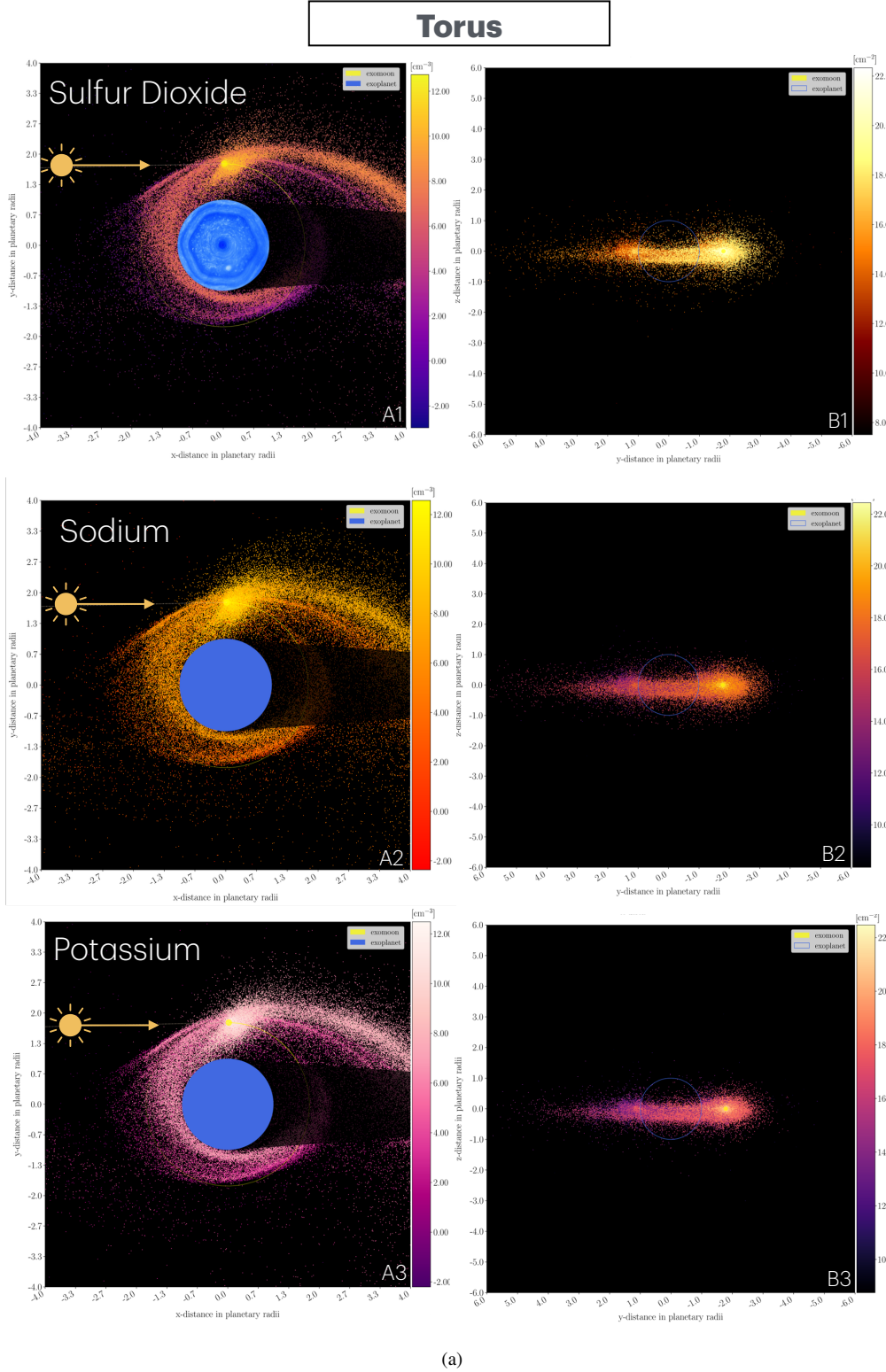
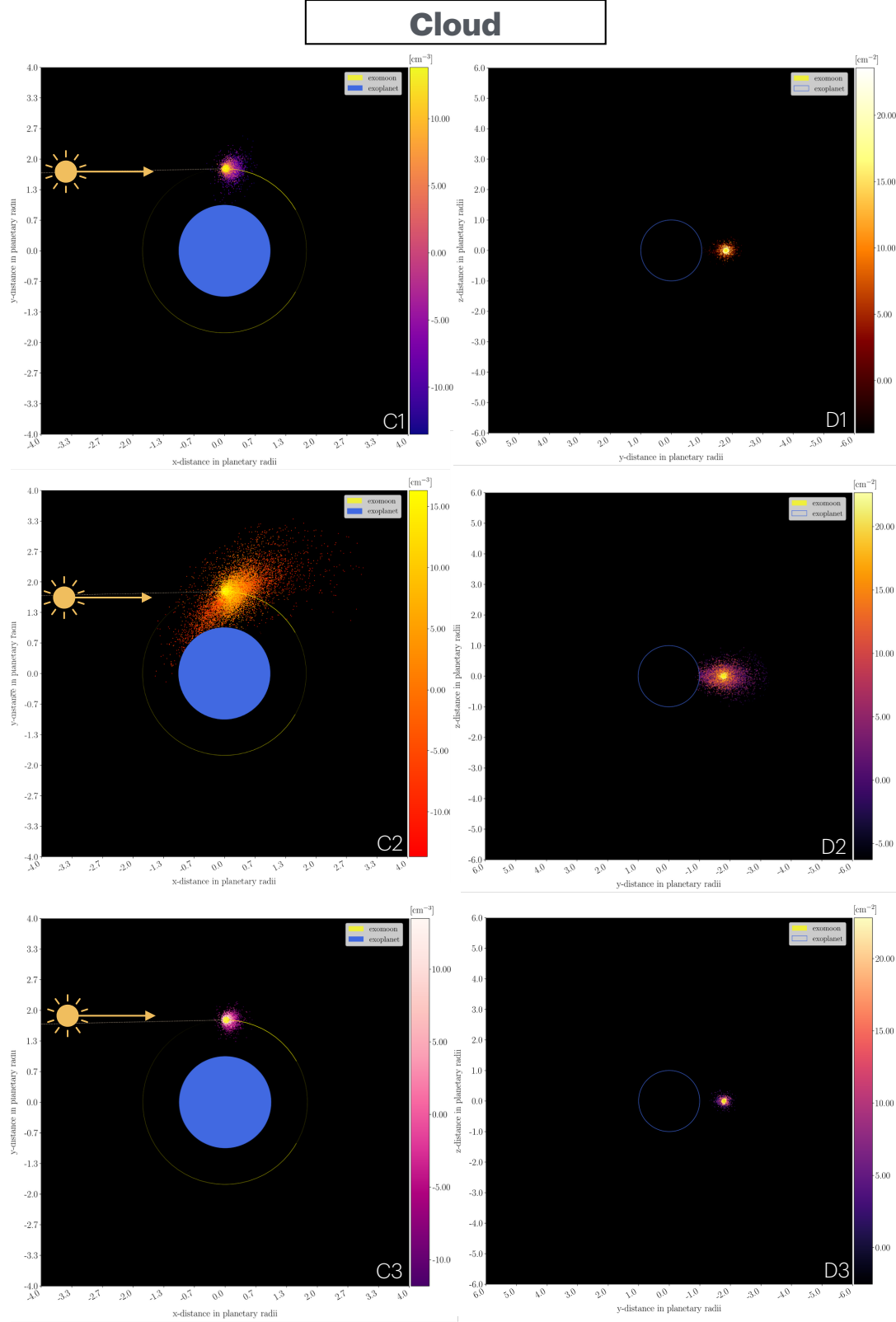


Figure 3. (a) *serpens* Monte-Carlo simulations of neutral SO_2 , Na, K around an *exo-Io* for a toroidal geometry. Top down (1st column: A1, A2, A3) and line-of-sight (2nd column: B1, B2, and B3) simulations. The approximate total number of particles reproducing the evaporative transmission spectra simulated by *prometheus* in Section 2 are: $N_{\text{Na}} = 10^{32.82}$, $N_{\text{K}} = 10^{32.97}$, and $N_{\text{SO}_2} = 10^{39}$ atoms/molecules in the system. Particles inside the exoplanet shadow have a lifetime of 3 hours for all cases.



(b) Cloud geometry. Top down (1st column: C1, C2, C3) and line-of-sight: (2nd column: D1, D2, and D3) simulations. Species lifetimes in the cloud scenario are limited by photoionization following [Huebner & Mukherjee \(2015\)](#); [Oza et al. \(2019\)](#). The exoplanet transit duration is given by $t_{1-4} = 2.8032 \pm 0.0192$ hours ([Faedi et al. 2011](#)). 1-D *serpens* cuts against observations representing minimum optically-thin column densities are described in Figure 4i (Na), 4ii (K), and 4iii (SO_2).

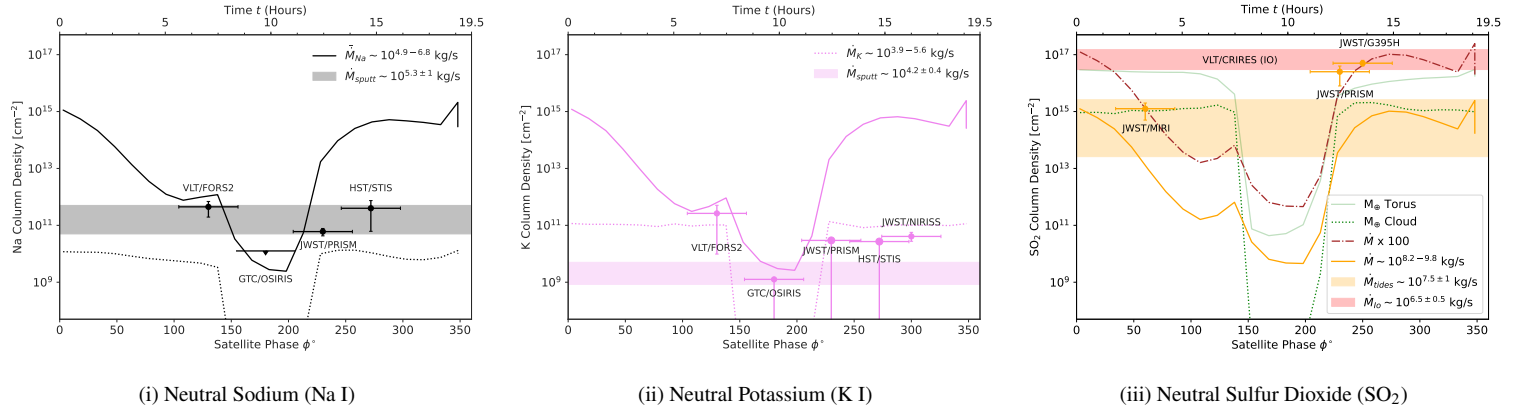


Figure 4. Minimum line-of-sight gas density variability of alkali metals and sulfur dioxide gas over several epochs. Data points: measurement from each instrument/epoch for Na (a black), K (pink), and SO₂ (orange). X-errors: transit duration (2.8 hours). Horizontal bands: 1-D predictions from 3-body tidal heating estimates by [Oza et al. \(2019\)](#) for Na (gray), K (pink), and SO₂ (orange), with Io’s observed column by VLT/CRIRES (red). Black, pink, orange lightcurves: 3-D Monte Carlo simulations ([Meyer zu Westram et al. 2024](#)) modelling sputtered clouds (dotted) and toroidal (solid) geometries. Panel iii: Green lightcurves: SO₂ simulations for an Earth-sized satellite cloud (dash-dot) and torus (solid). Brown dash-dot is $\sim 100\times$ Io torus scenario in orange.

variations in average particle densities \bar{n} primarily stem from radiative forces, resulting in minor fluctuations compared to the changes in average column densities \bar{N} . As lifetimes decrease further, particularly for K, evaporated material becomes increasingly confined to the exomoon, leading to a disappearance in line-of-sight signal during occultation. A prolonged species lifetime typically results in toroidal structures for small satellites. If the exomoon is massive the evaporated material may also return to the surface. These toroidal structures better distribute material along the orbit (similar to Io and Enceladus), which leads to less night-to-night variability while also increasing the total number of absorbing material. This is particularly interesting for SO₂, where column densities are large and more consistent between the data retrievals. Our torus simulations of SO₂ in Figure 3 suggest that column densities may vary by a significant amount but in a more controlled and continuous fashion. These trends are illustrated in Figure 4i, 4ii, and 4iii which show the temporal variability of integrated gas densities for Na, K, and SO₂ across different epochs and instruments as well as comparisons between simulated torus and cloud geometries under varying exomoon mass scenarios. We compute the maximum possible column density implied by a recent K I non-detection by Gran Telescopio Canarias (GTC)/OSIRIS ([Jiang et al. 2023](#)) in Figure 4ii. In contrast, a confined SO₂ cloud, strictly limited to the photoionization lifetime, can cause a complete loss of signal during exomoon occultation - more akin to something we expect for K. Furthermore, integrating the column density of a photoionization limited SO₂ cloud over the transit duration does not yield large enough values to explain what we see in data. Whether it is reasonable to assume a prolonged lifetime of SO₂ molecules at WASP-39 b is difficult to assess. Although we do not explicitly track ions, which are known to influence the Jupiter-Io plasma torus ([Bagenal 1994](#)), we calculate photoionization and electron-impact. The ionization rates imply a large presence of free electrons and SO₂ ions, which may boost the lifetime on the order of a transit duration.

4 CONCLUSIONS

Overall, we find that our numerical simulations in Figure 4 are able to reproduce observed column densities, suggesting that a natural satellite source may not be negligible. For instance, especially for the Na and SO₂ cases in Figure 4i & 4iii, a torus is required in comparison to cloud densities (dotted line) are far too small no matter the

mass of the unknown satellite. For Na an extended cloud, smaller than a torus, similar to the streams seen at Io approximates the epoch to epoch variability well. For K, since there is no identified KCl torus at Io, it may be possible that it is indeed a cloud, especially due to the disappearance of the K line completely in the JWST/PRISM data. Table 2’s mass loss ranges \dot{M} indicate that a Na & K torus is, in principle, able to be sustained based on JWST and VLT data of evolving absorption features from subtle alkali absorption (sputtered cloud geometry) to large transit depths (torus geometry). The $\dot{M}_\gamma - \dot{M}_{\text{tor}}$ values provide a range required to sustain N . Characterizing possible instrumental and stellar variability would benefit from dedicated repeat observations.

4.1 Volcanic Exomoon Output in Time and Mass Flux

Results from the *serpens* simulations reveal that mass-loss from an exomoon can produce strongly localised Na & K clouds. When integrating average Na column densities over the transit duration of ~ 2.8 hours, we are able to infer values comparable in magnitude to those in [Oza et al. \(2019\)](#). If K is locally bound to a putative exomoon, a natural explanation for a non-detection is the (partial) occultation of the satellite (and its exosphere) by the planet. Furthermore, as can be drawn from the phase-curve in Figure 4, a toroidal structure for SO₂ (green solid line) is better at explaining the subtly varying observational column densities while also providing large enough values when integrating over the transit duration. Sputtered clouds imply orders of magnitude variations, resulting in disappearances interpreted in Figure 4i and 4ii as alkali clouds, in contrast to the volcanic gas tori implying a more subtle variation between epochs ~ 20 . The behavior is further consistent with *prometheus* geometries of an exomoon cloud and tori reported in Table 1 and Figure 1.

The values inferred in Figure 4 offer a range of possibilities for a putative exomoon to source the volcanic gases detected in transmission. By considering a cloud or toroidal lifetime τ_i as described in Section 2 following $\dot{M} \sim mN\pi R_p^2/\tau_i$, we constrain roughly $\dot{M} \sim 10^{4.9-6.8}$, $10^{3.9-5.6}$, and $10^{8.2-9.8}$ kg/s for Na I (black), K I (pink), and SO₂ (orange) respectively, consistent with approximations predicted by [Oza et al. \(2019\)](#) (shaded regions) if a toroidal geometry is assumed ([Johnson et al. 2006b](#); [Meyer zu Westram 2023](#)). The green phase curve of an Earth-mass satellite, fits the data better than an Io-mass satellite (orange). Of course, it is also possible that a smaller satellite is interacting with the upper atmosphere of the gas

giant, similar to Enceladus and Io, as the escape would be far larger (Meyer zu Westram et al. 2024). In that case, the mass loss ranges may imply the putative satellite is in its last stage of evolution, on its way to transform into a ring satellite. Due to the favorable orbit of WASP-39 b, it may be that this satellite is still intact (Figure 5), and has not yet fully disintegrated at the Roche limit (blue vertical line). The preferred tidal Q value from Oza et al. (2019), red line in Figure 5 implies a migration time > 10 Gyrs to an orbit at the photosphere of ~ 8.07 h, assuring the survival of the satellite. The red band indicated in Figure 4 is the column density of Io, with the mass loss range of volcanism needed to supply it against atmospheric sputtering (Johnson 2004). Hot Saturns in addition to WASP-39 b have now been modeled in 3-D along with predictions of their NaD phase curves for HD209458 b, HD189733 b, WASP-49, WASP-96, WASP-69, WASP-17 b, XO-2N b, and HAT-P-1 b by Meyer zu Westram et al. (2024).

4.2 Outlook

Toroidal exosphere simulations from *serpens* and *prometheus* approximate a line-of-sight (LOS) column $N \sim 10^{16}$ SO_2/cm^2 from a tidally-heated outgassing rate predicted in previous modelling at $\sim 10^{8.5}$ kg/s. Surprisingly this minimum rate for a toroidal geometry, changes by an order of magnitude for SO_2 as well, suggesting an exogenic process. The SO_2 column is nearly identical to Io's, whose disk is covered in infrared-bright features near $4 \mu\text{m}$ (Carlson et al. 1997) and $7.3 \mu\text{m}$ as seen by ongoing *Juno/JIRAM* (Tosi et al. 2020) & *JWST/MIRI* observations (de Kleer et al. 2023). Evaluating Na/SO_2 , the neutral observations vary from ~ 2500 to $10 \times$ less than Io's known $\chi_{\text{NaCl}/\text{SO}_2}$ abundance (Lellouch et al. 2003), likely due to enhanced escape and heating beyond 1100 K. Interestingly, the Roche limit for a rock is interior to the planetary surface, therefore atmosphere/exosphere interactions are especially important at this system. To constrain putative satellite orbits, high-resolution alkali Doppler shift observations are required (Oza et al. 2024; Unni et al. 2025). Since volcanic gas is expected to be accompanied by dust, recent *JWST* mid-infrared observations are further suggestive of a natural satellite at this alkali hot Saturn system (Flagg et al. 2024) as well as other hot Jupiter systems studied in Oza et al. (2019) such as HD-189733 b (Inglis et al. 2024).

Acknowledgments

A.V.O thanks H. Knutson for valuable insight on HST/STIS and N. Nikolov on VLT/FORS2 data. The research described in this paper was carried out in part at the Jet Propulsion Laboratory, California Institute of Technology, under a contract with the National Aeronautics Space Administration. © 2025. All rights reserved. Y.M. acknowledges support from the European Research Council (ERC) under the European Union's Horizon 2020 research and innovation programme (grant agreement no. 101088557, N-GINE).

DATA AVAILABILITY

Relevant *JWST* data used in this study can be accessed through the Space Telescope Science Institute (STScI) archive at <https://archive.stsci.edu>.

REFERENCES

Ahrer E.-M., et al., 2023, *Nature*, **614**, 653
 Alderson L., et al., 2023, *Nature*, **614**, 664
 Ashton E., Gladman B., Alexandersen M., Petit J.-M., 2025, *Research Notes of the American Astronomical Society*, **9**, 57

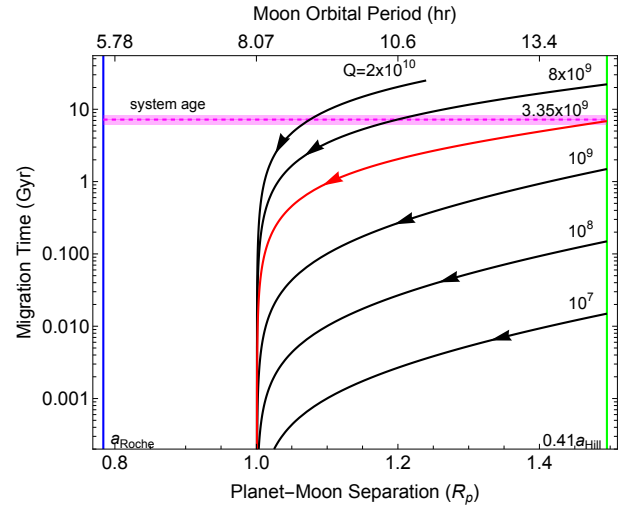


Figure 5. Moon migration plot for an exo-Io orbiting WASP-39 b. Each curve represents the time it takes for the moon to migrate due to equilibrium tides from a certain initial separation to the surface of the planet, for a given Q of the planet. The red curve pertains to the estimated Q of WASP-39 b based on the analysis in Oza et al. 2019. We assume the moon orbits faster than the planet spins, so that the moon falls towards the planet (towards the left of the plot). The pink region is the estimated age range of the system, at 7.2 Gyr. The vertical lines represent the Roche limit (blue) and Hill sphere (green).

Bagenal F., 1994, *J. Geophys. Res.*, **99**, 11043
 Bello-Arufe A., et al., 2025, *ApJ*, **980**, L26
 Carlson R. W., et al., 1997, *Geophys. Res. Lett.*, **24**, 2479
 Cassidy T. A., Mendez R., Arras P., Johnson R. E., Skrutskie M. F., 2009, *ApJ*, **704**, 1341
 Charnoz S., Canup R. M., Crida A., Dones L., 2018, *The Origin of Planetary Ring Systems*, pp 517–538, doi:10.1017/9781316286791.018
 Draine B. T., 2011, *Physics of the Interstellar and Intergalactic Medium*
 Faedi F., et al., 2011, *A&A*, **531**, A40
 Fegley B., Zolotov M. Y., 2000, *Icarus*, **148**, 193
 Feinstein A. D., et al., 2023, *Nature*, **614**, 670
 Fischer P. D., et al., 2016, *ApJ*, **827**, 19
 Flagg L., et al., 2024, *ApJ*, **969**, L19
 Foreman-Mackey D., Hogg D. W., Lang D., Goodman J., 2013, *PASP*, **125**, 306
 Fournier-Tondreau M., et al., 2025, *MNRAS*,
 Gebek A., Oza A. V., 2020, *MNRAS*, **497**, 5271
 Gibson N. P., de Mooij E. J. W., Evans T. M., Merritt S., Nikolov N., Sing D. K., Watson C., 2019, *MNRAS*, **482**, 606
 Herrick R. R., Hensley S., 2023, *Science*, **379**, 1205
 Huebner W. F., Mukherjee J., 2015, *Planet. Space Sci.*, **106**, 11
 Inglis J., et al., 2024, *ApJ*, **973**, L41
 Jiang C., Chen G., Pallé E., Murgas F., Parviainen H., Ma Y., 2023, *A&A*, **675**, A62
 Johnson R. E., 2004, *ApJ*, **609**, L99
 Johnson R. E., Huggins P. J., 2006, *PASP*, **118**, 1136
 Johnson R. E., Strobel D. F., 1982, *J. Geophys. Res.*, **87**, 10385
 Johnson R. E., et al., 2006a, *Icarus*, **180**, 393
 Johnson R. E., Smith H. T., Tucker O. J., Liu M., Burger M. H., Sittler E. C., Tokar R. L., 2006b, *ApJ*, **644**, L137
 Kisare A. M., Fabrycky D. C., 2024, *MNRAS*, **527**, 4371
 Kleisioti E., Dirkx D., Rovira-Navarro M., Kenworthy M. A., 2023, *A&A*, **675**, A57
 Kleisioti E., Dirkx D., Tan X., Kenworthy M. A., 2024, *arXiv e-prints*, p. arXiv:2405.01970
 Lellouch E., Paubert G., Moses J. I., Schneider N. M., Strobel D. F., 2003, *Nature*, **421**, 45
 Lellouch E., Ali-Dib M., Jessup K.-L., Smette A., Käufel H.-U., Marchis F.,

- 2015, *Icarus*, **253**, 99
- Mahieux A., et al., 2023, *Icarus*, **399**, 115556
- Meyer zu Westram M., 2023, SERPENS - Simulating the Evolution of Ring Particles Emergent from Natural Satellites, doi:10.5281/zenodo.8353170, <https://github.com/momzw/SERPENS>
- Meyer zu Westram M., Oza A. V., Galli A., 2024, *Journal of Geophysical Research: Planets*, **129**, e2023JE007935
- Narang M., Oza A. V., Hakim K., Manoj P., Banyal R. K., Thorngren D. P., 2023a, *AJ*, **165**, 1
- Narang M., et al., 2023b, *MNRAS*, **522**, 1662
- Nikolov N., et al., 2016, *ApJ*, 832
- Oza A. V., et al., 2019, *ApJ*, **885**, 168
- Oza A. V., et al., 2024, *ApJ*, 973, L53
- Patel J. A., et al., 2024, *A&A*, **690**, A159
- Peale S. J., Cassen P., Reynolds R. T., 1979, *Science*, **203**, 892
- Powell D., et al., 2024, *Nature*, 626, 979–983
- Quick L. C., Roberge A., Mlinar A. B., Hedman M. M., 2020, *PASP*, **132**, 084402
- Reif F., 1965, *Fundamentals of Statistical and Thermal Physics*. McGraw-Hill, New York
- Rustamkulov Z., et al., 2023, *Nature*, **614**, 659
- Schmidt C., et al., 2023, *PSJ*, **4**, 36
- Sheppard S. S., et al., 2018, *Research Notes of the American Astronomical Society*, **2**, 155
- Sheppard S. S., Tholen D. J., Alexandersen M., Trujillo C. A., 2023, *Research Notes of the American Astronomical Society*, **7**, 100
- Sing D. K., et al., 2016, *Nature*, 529
- Smyth W. H., Combi M. R., 1988, *ApJ*, **328**, 888
- Sulcanese D., Mitri G., Mastrogiuseppe M., 2024, *Nature Astronomy*, Tennyson J., et al., 2024, *J. Quant. Spectrosc. Radiative Transfer*, **326**, 109083
- Tokadjian A., Piro A. L., 2023, *AJ*, **165**, 173
- Tosi F., et al., 2020, *Journal of Geophysical Research (Planets)*, **125**, e06522
- Tsai S.-M., et al., 2023, *Nature*, **617**, 483
- Unni A., et al., 2025, *MNRAS*, *in press*
- Veeder G. J., Matson D. L., Johnson T. V., Blaney D. L., Goguen J. D., 1994, *J. Geophys. Res.*, **99**, 17095
- Wakeford H. R., et al., 2018, *AJ*, **155**, 29
- Wilson J. K., Mendillo M., Baumgardner J., Schneider N. M., Trauger J. T., Flynn B., 2002, *Icarus*, **157**, 476
- Yang J., Hu R., 2024, *ApJ*, **966**, 189
- Yung Y. L., Demore W. B., eds, 1999, *Photochemistry of planetary atmospheres*
- de Kleer K., et al., 2023, Mass-loss from Io's volcanic atmosphere: A unique synergy with the Juno Io fly-by, JWST Proposal. Cycle 2, ID. #4078

This paper has been typeset from a \LaTeX file prepared by the author.